Spatial Quantification of Microstructural Degradation during Fast Charge in 18650 Lithium-Ion Batteries Through Operando X-Ray Micro Tomography and Euclidean Distance Mapping

Eva M. Allen<sup>a,g</sup>, Linda Y. Lim<sup>b,c</sup>, Albert Liu<sup>b,d</sup>, Michael F. Toney<sup>e,f</sup>, Jordi Cabana<sup>a,\*</sup>, and Johanna

Nelson Weker<sup>f</sup>

<sup>a</sup> Department of Chemistry, University of Illinois at Chicago, Chicago, IL, 60608 USA

<sup>b</sup> Lucid Motors, Newark, CA, 94025, USA

<sup>c</sup> School of Computer Science, Georgia Institute of Technology, Atlanta, GA, 30332 USA

<sup>d</sup> Ample Inc, San Francisco, CA, 94124, USA

<sup>e</sup> Department of Chemical Engineering, University of Colorado, Boulder, Co, 80309, USA

<sup>f</sup> Stanford Synchrotron Radiation Lightsource, SLAC National Accelerator Laboratory, Menlo
Park, CA, 94025, USA

<sup>g</sup> Argonne National Laboratory, Lemont, IL, 60439

\*Corresponding Author Contact Information: Email: jcabana@uic.edu, Phone: (+1) 312-355-

4309

Abstract: Fast charging at rates above 1C aggressively accelerates structural degradation induced

by increases in local temperature and inhomogeneous transport of charge. At the micron scale, the

first indication of damage is irreversible expansion of the electrode layers. Electrode damage often

involves void formation between the active material and conductive-binder matrix. Quantification

of this evolution must be carried out in real-time and, thus, non-destructively. We report the

operando X-ray microtomography of cylindrical cells under fast charge cycling. Two 18650

batteries were measured during cycling after antecedent fast charging cycles to track

morphological damage at different points of battery life. A method of deep learning segmentation

was used to objectively quantify the electrode degradation. Using Euclidean Distance Mapping,

electrode dilation and voids were spatially resolved. Highly reversible trends in dilation were

quantified during charge/discharge in the anode layers with irreversible increases in electrode

voids. Anode voids showed clear localization within the first 10 µms near the current collectors,

indicating delamination, that spread upon further cycling. The cathode dilation trended opposite

to the anode with higher fluctuations and an overall decrease in cathode voids. Insight into how

fast charging induces structural damage better informs research into fast-charge protocols and new

battery chemistries.

Keywords: Lithium-ion battery; Operando; Microcomputed tomography; Fast charge; Deep

learning; Electrode dilation

2

#### 1. INTRODUCTION:

The growing popularity of fully electric vehicles (EVs) anticipates a high demand for rechargeable lithium-ion batteries (LiBs). EVs require a battery that can reversibly undergo faster charging, at rates above 1C, defined as the current at which it takes one hour for a battery to charge/discharge to full capacity. This performance requirement is essential in the broader commercialization of EVs, given consumer expectations and habits from the use of combustion counterparts. Unfortunately, fast charging has been shown to induce aggressive morphological degradation that unacceptably compromises the capacity retention of the battery. High rates of charge induce gradients of diffusion of Li<sup>+</sup> ions into the electrode architecture, which is typically a porous composite that is tens of µm thick. The resulting gradients in electrode utilization produce large anisotropic volume changes at both the anode and cathode.<sup>1,2</sup> Such gradients in stress can lead to increased particle cracking at the surface near the separator compared to the bulk structure of the electrode.<sup>3–5</sup> Another common effect is void formation both within the active material and with respect to the conductive binder matrix (CBM), creating pockets of electronic isolation.<sup>6–8</sup> In extreme cases, these volume changes can cause delamination of the electrode coating from the current collecting foil. The resulting loss of conductivity and connections between active material have high costs in the overall lifetime of the battery. Understanding the evolution of the microstructure inside the battery could inform strategies to bypass this damage while enabling the desired fast cycling rates. Ideally, such evolution would be quantified in real-time without requiring battery modifications in the process.

In the following study, operando X-ray microcomputed tomography (microCT) was used to track the dilation of the electrode layers while spatially pinpointing contributing factors to irreversibility, such as void formation and delamination, during cycling of an 18650 battery after prior high-rate charge cycling. X-ray microCT has grown in popularity to diagnose degradation

and other internal processes in Li-ion batteries. 8–10 MicroCT is a technique of choice because it is non-destructive, and it combines the ability to collect large fields of view with high spatial and temporal resolution. A typical 18650 cell architecture consists of both anode and cathode dual-coated on long copper and aluminum foil strips, respectively. The anode and cathode strips are sandwiched between layers of porous polymer separators and wound together into a jellyroll, creating a structure of repeating layers across the cell. In X-ray microCT, any voids appear as darker pixel regions in the electrode coating distinct from the lighter CBM shown in Figure S1.

For the accurate quantification of the various internal battery components and evolution of degradation, semantic segmentation needs to be accomplished. Semantic segmentation refers to labeling individual pixels of an image to a corresponding classification.<sup>11</sup> Otsu thresholding methods<sup>12</sup> of segmentation may be used in segmenting out the copper current collectors (Cu CCs), which display the highest intensity. Still, this method and other basic mathematical segmentation methods quickly fail when segmenting the other battery components. Accurate segmentation of the six elements of interest: anode, cathode, copper, and aluminum current collectors (Al CCs), anode, and cathode void regions require more user-defined insight into battery morphology. Nuanced manual morphological-based segmentation of this type would quickly become unfeasible at the scale necessary to fully segment a complete 3D tomogram of 1024 slices, let alone the many tomograms that make up each operando cycling series in this study. Alternatively, deep learning is a method that iteratively learns from data using algorithms, allowing for the automatic formulation of essential features that define accurate segmentation of each classification component.<sup>13</sup> While deep learning segmentation is gaining popularity in battery imaging, most studies focus on two-component systems, void and solid material classifications, lumping together cathode, anode, and their respective current collectors.8 Greater insight into microstructural

degradation is gained through the full segmentation of all battery components based on morphological considerations.

To establish the spatial dependence of induced voids, many researchers have used methods relying on average intensity changes sampled using various data sectioning methods<sup>14</sup>, such as intensity line scans<sup>10</sup> or serial sectioning of equidistant strips. <sup>15</sup> These methods present issues when intensity differences can be a symptom of other reconstruction artifacts, sample collection conditions, or other intensity changes of neighboring features. Here, we offer an alternative method to spatial quantification, Euclidean Distance Mapping (EDM). EDM is used widely in computer vision applications, such as pattern recognition and robotics 16, and battery applications to calculate particle sizes. 17-19 Euclidean distance is the measurement between two points, but in the case of three-dimensional objects, EDM takes into account the three-dimensional morphology of the reference component to provide the relative spatial positioning of the other segmented components. For our purposes, the current collectors were used as the reference components. The basic principle of EDM uses a distance transform to convert a binary segmentation mask consisting of background and foreground pixels into a greyscale gradient map (Figure 1d). The pixel brightness value equals the shortest distance from the nearest foreground pixel. This map is then used to track the other segmentation components spatially in the three-dimensional data set. The EDM method uses the full pixel resolution and entire data set of the microCT method to track components indicative of degradation and capacity fade spatially without additional processing time.

In addition to electrode void positioning, EDM was used to track the reversible and irreversible dilation and contraction of the anode and cathode electrode coating layers upon Li-ion de/intercalation (Figure 1d). This application presents an alternative to traditional dilatometry

experiments previously limited to soft-walled pouch cells where electrode expansion and contraction are tracked externally. The limitation of conventional setups ignores significant contributions of cell architecture on the internal degradation of reversible electrode volume changes. While calculations of electrode thickness in CT data can be accomplished using thickness mesh calculations<sup>20</sup>, this method relies on the surfaces of segmentation components by calculating the distance between boundary points where the greatest extent of segmentation error occurs.<sup>21</sup> MicroCT, in combination with the deep learning segmentation and EDM, can allow for the flexibility needed to observe and quantify thickness changes in hard-walled battery architectures, such as cylindrical 18650 cells in situ. Both anode and cathode volume contributions are measured simultaneously without tedious manual measurements.<sup>22</sup> Finally, this method will allow for direct visualization of other degradation processes that contribute to thickness changes like electrode delamination, particle rearrangement, and void formation, which will be explored in the subsequent sections.

Deep learning segmentation and EDM provide a path forward in exploring how fast charge induces morphological changes that lead to capacity fade and battery failure providing the tools necessary to begin to mitigate these processes. By implementing technical solutions to the challenges of data analysis outlined, this study is the first instance of a six-component deep learning segmentation model applied across multiple operando charge-discharge cycles in a cylindrical cell format. We also present a new methodology to calculate reversible/irreversible expansion and contraction of individual electrode layers during an operando experiment for direct observation of the morphological processes governing this sign of degradation. Developing these faster, more comprehensive data analysis techniques makes operando studies of batteries more meaningful by moving beyond qualitative observational changes to quantifiable comparisons.

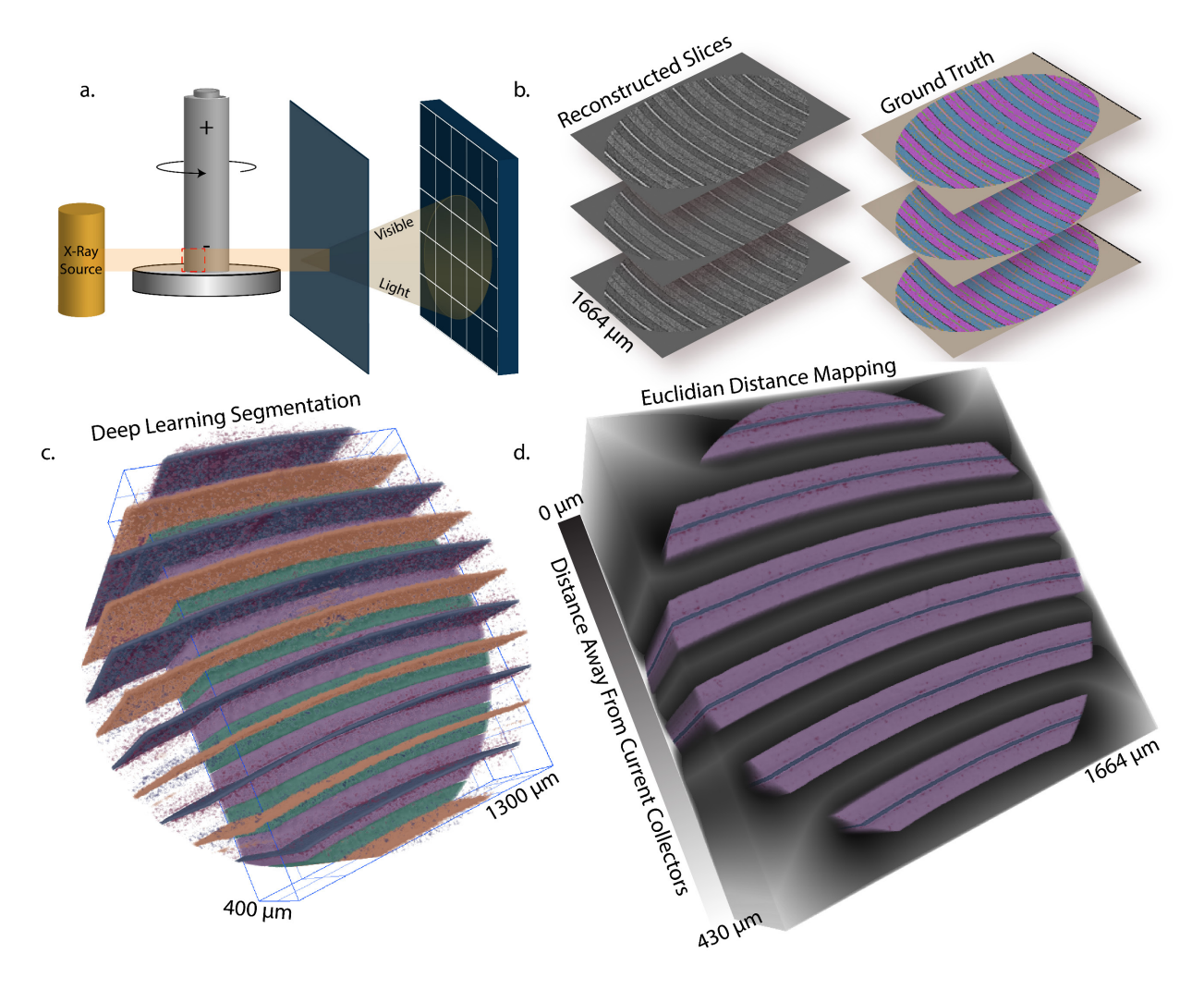


Figure 1. (a) Micro-computed tomography collection of an 18650-battery showing the approximate field of view used. (b) Reconstructed slices from collected projection files (left). Hand segmented slices used for training data for the U-Net segmentation model (right). (c) Segmentation model applied to a three-dimensional tomogram. Cathode (teal) and anode (purple) coatings are eroded to show internal voids and Al (orange) and Cu (blue) CCs. (d) Euclidean distance transform mapping applied to the 3D dataset using the Cu CCs as the reference point.

## 2. EXPERIMENTAL:

2.1. Operando Micro Computed Tomography of Fast Charge Cycling of 18650 Batteries.—
Two commercial 18650 batteries consisting of a LiNi<sub>0.8</sub>Co<sub>0.15</sub>Al<sub>0.05</sub>O<sub>2</sub> (NCA) cathode, multilayer polymer separator, and graphite anode were cycled using a voltage window of 2.5 to 4.2 V

under simulated fast charging conditions using a MACCOR cycler. The cycling rates used prior to the operando collection were a 3C charge and a 1C discharge, the rates were reduced during collection. The cells were received after initial formation cycling, this state is referred to as "asreceived" in the rest of the paper. The as-received anode and cathode electrodes were approximately 60 μm in thickness for each coating layer. The thicknesses of the current collectors were 10 μm and 12 μm for Cu and Al, respectively. One cell was monitored during the 3<sup>rd</sup> cycle and the other during the 81<sup>st</sup> and 82<sup>nd</sup> cycles in the operando study. The cells were cycled during the microCT data collection at beamline 2-BM at the Advanced Photon Source at Argonne National Laboratory. The x-ray energy was >70 keV using the pink beam from the bending magnet. The collection time for each tomogram was approximately 4 min with no delay between tomograms. The pixel size was 0.65 μm with an achieved imaging resolution of around 3 μm. Tomographic reconstruction was accomplished using the python package Tomopy<sup>23,24</sup> with the Gridree<sup>25</sup> reconstruction algorithm.

2.2. Quantification of MicroCT Data Through Deep Learning Segmentation.—
The segmentation process was accomplished through the open-sourced software, Dragonfly, an advanced imaging tool from Object Research Systems (ORS) specialized in 3D data set rendering, post-image processing, and image segmentation. Dragonfly allows for the creation of training data, training of a Convolutional Neural Network (CNN) segmentation model, which utilizes Compute Unified Device Architecture (CUDA) fast processing, and implementation and analysis of the CNN on a 3D dataset entirely through a graphical user interface (GUI). Training data were created with a set of 17 hand-segmented reconstructed microCT slices (Figure 1b). These binary masks were created using threshold-guided painter tools. Seven target components were chosen to be segmented: The anode and cathode electrode coatings, the corresponding anode and cathode internal voids, Cu and Al CCs, and the circle mask that was applied over partial volume artifacts

appearing around the field of view edges. The polymer separators were excluded from the segmentation model but were the only component in the background class. For example, while the morphology of the carbon and binder matrix (CBM) in the cathode electrode coating layers is below the resolution limit of the microCT experiment, it appears as darker intensity regions between the higher intensity cathode secondary particles. Careful comparison of the as-received and cycled 18650 microCT data allow the user to differentiate between the cycling-induced voids and CBM (Figure S1). By observing the changes in texture, morphology, and intensity from the as-received to the cycled data, rules were established to define the hand-segmentation of the void class for the electrodes for the model training dataset. 20% of the training data was used for validation during training. A categorical cross-entropy loss function was used to evaluate training progress. A series of data augmentation layers were applied during model training: horizontal and vertical flip, rotation, shear, brightness, and gaussian noise. A U-Net<sup>26</sup> deep learning architecture was trained for a total of 45 epochs, stopping when no improvement of loss was observed. All other deep learning parameters can be found in Supplementary Table S1.

Before applying the segmentation model, the greyscale intensity histograms were normalized to each other. Application of the segmentation model on 500 slices with dimensions of 2560 x 2560 pixels takes approximately 20 minutes using a computer with 64 GB of RAM, an AMD Ryzen 7 1700X Eight-Core Processor, and an NVIDIA GeForce GTX 1060 6GB GPU. The performance of the segmentation model for each component was evaluated using various standard evaluation metrics calculated from total false positive/negative and true positive/negative pixel values extracted from the comparison of the ground truth and model output binary masks through a confusion matrix.<sup>27</sup> These scores are reported in Figure S2. Maps of the segmentation model false

positive and negative pixel values overlaid on the greyscale data are reported in Figure S3, showing most of the segmentation model error occurs at the interfaces of the components.

After applying the segmentation model, the CC segmentation class was itemized using a connected-components analysis. Itemization through connected-component labeling allows the separation of a segmentation class by setting a maximum value of voxel connectivity. A six-connectivity value was used for the current collectors, meaning that any region of the CC class that was connected by less than that voxel value was separated into an individual class. Upon visual inspection, the number of separated CC layers were counted within the 3D volume. For example, if six CC layers were present within the FOV, then the first six CC components of highest volume were separated as a new single class and all other smaller volume segmentation components were deleted. This process was essential to remove minor false positive segmentation errors shown in Figure S3 that would skew the EDM. The EDM was applied using the CC class as the starting reference point, or distance zero. Each voxel outside the CC class was replaced by a grey value equal to the voxel distance away from the nearest neighboring voxel. This calculated distance map was then used as a reference to measure how internal components of the 18650 batteries evolve spatially during cycling.

## 3. RESULTS AND DISCUSSION:

3.1. Euclidean distance mapping for operando dilatometry in 18650 cells.— Figure 1a shows the microCT experimental setup. A lower portion of the two 18650 batteries is chosen for all operando imaging experiments, furthest away from the current collecting tabs, near the negative terminal, and approximately 4 mm out from the jellyroll core. This region is used to avoid the non-uniform thermal distribution near the current collecting tabs that causes higher localized delamination during fast-charge. Approximately 20 tomograms are collected for each

charge-discharge cycle set. After X-ray projection images are gathered, they are reconstructed into cross-sectional slices in the XY plane shown in Figure 1b.

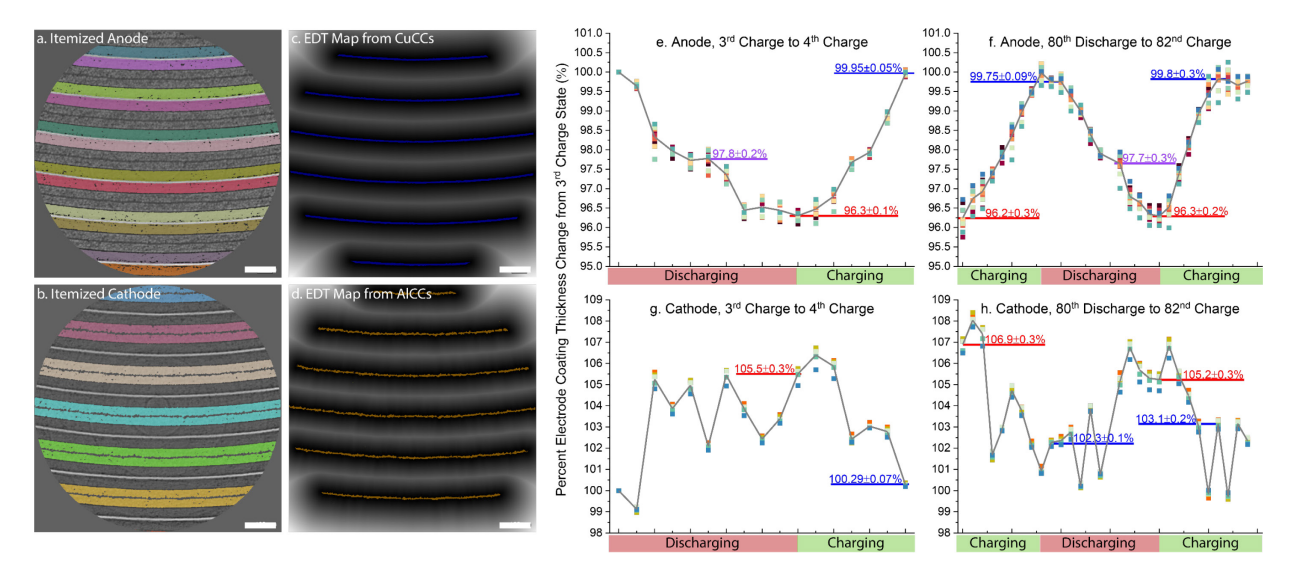


Figure 2. Thickness tracking of electrode layers using EDM. (a) Itemized segmentation of individual layers of anode coatings and (b) double-coated layers of the cathode. Electrode color indicates component separation. Calculated Euclidean distance map (EDM) from the segmentation layers of the (c) Cu CCs and (d) Al CCs. Evolution of the thickness of anode and cathode is measured, operando, from the 3<sup>rd</sup> charge to the 4<sup>th</sup> charge (e and g) and 80<sup>th</sup> discharge to 82<sup>nd</sup> charge (f and h). Multiple points are reported for each cycling position and are representative of the itemized electrode layers and are shown in various colors. Each point along the x-axis is a separate tomogram with a collection time of ~4 min, there is no delay between each collection, the charging and discharging state is indicated. Values of thickness are calculated from the corresponding EDM using the mean EDM pixel value perpendicular to the Cu (anode) and Al (cathode) current collector layers. All values in the graphs are normalized to the 3<sup>rd</sup> charge. The grey trendline indicates the average percent thickness change calculated from the electrode layers. Percentages at the end of

charge (blue), discharge (red), and intermediate state of the anode (purple) are labeled. Scale bars =  $200 \ \mu m$ .

An EDM method is established to gain insight into whether a rigid cylindrical cell format can constrain electrode expansion, in comparison to complementary dilatometry experiments with soft-walled pouch cells, while removing the expansion error of the other cell components. After the segmentation model is applied, subsequent masks are itemized via a component labeling function with a six-connected pixel value. Figure 2 shows, with color, the itemization of the electrode coating layers, anodes in panel a, and cathode in panel b. The itemization of the electrode layers provides a view of the spread in deviation of the thickness measurements. The individual anode layers on either side of the Cu CCs are easily separated using this method. However, the Al CCs do not provide an explicit boundary to separate the individual cathode coating layers. The dual coatings sampled together are used to calculate the thickness change. The Cu and Al CCs are used to generate the EDM gradient plots for the anode and cathode layers, respectively, shown in Figure 2c and d. The expansion and contraction of the layers are calculated in the direction perpendicular to the current collectors, where the reference points are established. The mean distance away from the current collectors is used to track the change in thickness instead of the maximum distance to account for any minor false positives and negatives that may appear in the segmentation around the edge of the electrode components, shown in Figure S3. Thickness results are reported as percentages normalized to the value from the 3<sup>rd</sup> charge state, the first data point in Figure 2e and g for both anode and cathode, respectively. Visualization of the expansion and contraction of the electrode layers can be seen in the provided supplemental videos.

The average change in thickness of the anode layers in the 3<sup>rd</sup> to the 4<sup>th</sup> charge indicates highly reversible contraction and dilation. The average contraction of the individual layers during the 4<sup>th</sup> discharge is 3.7%, returning to 99.95±0.05% of the original volume upon charge. Despite only 88% capacity remaining from the as-received state, similar contraction is observed upon the 80<sup>th</sup> discharge, with a return to 99.75±0.09% of the original thickness during the 81<sup>st</sup> charge. Greater loss in reversibility is observed subsequently, with a 3.5% contraction during the 81<sup>st</sup> discharge and a smaller return to 99.8±0.3% of the original volume upon the 82<sup>nd</sup> charge. These observations agreed with a dilatometry study by Michael et al., where an average change in thickness of 3.8% thickness was found in the graphite anode after formation cycling.<sup>29</sup>

Two distinct regions of change are observed during discharge in Figure 2e. First, a 2.2% contraction led to a plateau indicated by the purple line, followed by another 1.5% contraction to the final plateau indicated by the red line. These distinct features correspond well to the phase transitions outlined in traditional dilatometry experiments by Michael et al.<sup>29</sup> and Bauer et al.,<sup>30</sup> which are found to correlate with the formation of different stages of graphite, governed by x in Li<sub>x</sub>C<sub>6</sub>. The same plateau regions are observed upon charge and further cycling in Figure 2f, but the feature is reduced, and higher linearity is observed, which could be a symptom of the reduced capacity in the  $80^{th}$  cycle.

In most traditional dilatometry experiments, the evolution of the cathode contribution is often ignored because it is assumed to be a magnitude less than the anode. MicroCT with EDM allows for measuring the cathode volume changes simultaneously and deconvoluted from the anode. In general, expansion and contraction are found upon discharge and charge, respectively (Figure 2g and f), in line with expected trends. The plot profiles are strikingly different from the anode graphs showing a pronounced reduction in linearity with distinct oscillations in thickness. The trends in

cathode thickness are confirmed with the voxel volume tracking graphs provided in Supplementary Figure S4. The comparison demonstrates that the trends are not skewed by the EDM or the minor segmentation error shown in S2 and S3. We posit that the irregular, lower resolution trends reflect a complicated convolution of factors due to the anisotropic atomic changes and particle rearrangement that the cathode undergoes during cycling, as opposed to the more linear changes at the anode. <sup>31</sup>

The contraction and expansion of the cathode electrode coatings Figure 2g and f, while significantly less clear than the anode, generally show a reversible contraction from the 3<sup>rd</sup> charge to the 4<sup>th</sup> charge and 80<sup>th</sup> discharge to the 82<sup>nd</sup> charge. At the 81<sup>st</sup> charge in Figure 2h, the baseline thickness is shifted up by about 2%, which could be due to cell-to-cell variation between the two cells used in this study. A further increase to 3% upon 81<sup>st</sup> discharge is calculated.

# 3.2. Degradation and Void Totals in Electrodes.—

After the model for deep learning, segmentation is applied to the tomograms of the as-received cell and along the charge-discharge curves, the voxel volumes assigned to the total electrode and void components are collected.

Void percentages are calculated using Eq. 1:

$$Voids (\%) = \frac{V_{Voids}}{V_{Elec} + V_{Voids}} \times 100\%$$
 (1)

to compare fluctuations across different cycling points (Figure 3), where  $V_{Elec}$  and  $V_{Voids}$  are the total volumes of pixels segmented as cathode or anode and their respective voids. The pixels segmented as Al and Cu CCs are not included in the calculation.

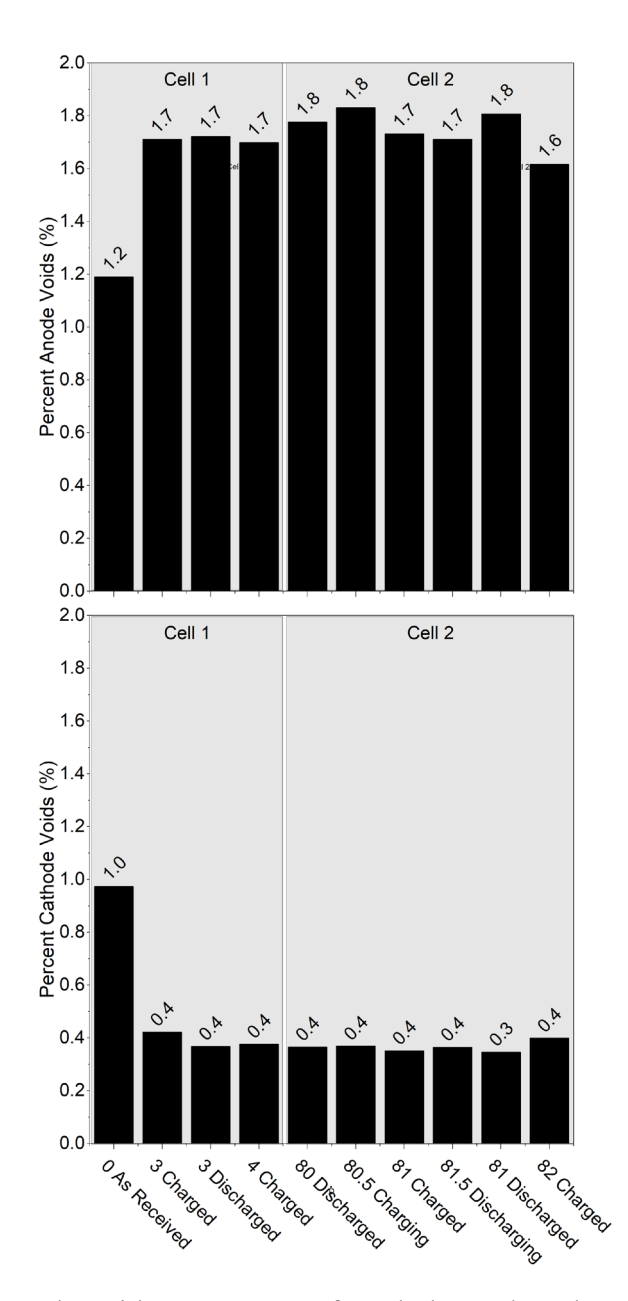


Figure 3. Cathode and anode void percentages of total electrode volumes from the pristine state and different cycling points across the 3<sup>rd</sup> to 4<sup>th</sup> cycle and 80<sup>th</sup> to 82<sup>nd</sup> cycle. The percentages are collected from two different 18650 cells of the same location, chemistry, and cycling parameters.

The initial percentage of the volume occupied by voids in the anode is 0.2% higher than the cathode (Figure 3). It is important to note that the void fraction need not represent total electrode porosity since much of it is under the spatial resolution of the microCT. The existing voids were

most likely introduced during the electrode and cell manufacturing and formation cycling undergone by the cell before being received for imaging.<sup>34</sup> After the 3<sup>rd</sup> charge state, an increase of 0.5% of voids is calculated for the anode. This increase could be associated with strain buildup due to gradients in the state of charge due to mass transport limitations.<sup>35</sup> The anode void totals remain stable through the 3<sup>rd</sup> charge to 4<sup>th</sup> charge at 1.7%. At the beginning of the 80<sup>th</sup> cycle, there is a small increase to 1.8%, with a slight reduction to 1.7% and 1.6% at the 81<sup>st</sup> and 82<sup>nd</sup> charge states. Since these changes are within the significance of the measurement, we speculate that the reduction of voids at the fully charged state could be associated with the swelling of the electrode at full lithiation, which reduces the volume of the void network.

The cathode void percent totals can be seen in Figure 3b. A decrease of 0.6% is calculated after the 3<sup>rd</sup> charge. The decrease in porosity can be explained through a few different mechanisms. First, volume changes in the electrode upon charge-discharge cause the active material and carbon matrix to rearrange<sup>29,33</sup>, filling some of the initial porosity, which could be pronounced enough to minimize changes in total thickness. This reordering has been seen in studies of silicon anodes, known for substantial swelling.<sup>32,33</sup> While, in comparison, NCA particles will not swell to the extremes of silicon, it is considered a plausible explanation for the irreversible decrease in porosity seen here and has previously been reported for LiCoO<sub>2</sub>.<sup>33</sup> In particular, the micron-sized secondary particles are prone to microcracking due to increased strain from inhomogeneous lithium diffusion during high charge rates. The fragments of broken secondary particles could fill the initial porosity of the electrode coating. There is no further reduction of total voids during additional cycling with only a slight drop down to 0.3% at the 81<sup>st</sup> discharge, most likely due to the dilation of the electrode, as the total returns to 0.4% upon charge.

3.3. Spatial Mapping of Electrode Voids using Euclidean Distance Transforms.—
While broad trends can be visualized using void totals, further insight must be gained into the specific spatial location where these voids occur in the electrode. Since the EDM method proves useful in showing trends in the dilation and contraction of the electrode coatings, the voids can be tracked using the same gradient maps generated from the current collectors. The positioning of individual voids is accomplished through the itemization of the anode and cathode void classes using the component labeling function previously described with a higher threshold of 26 points of pixel connectivity.

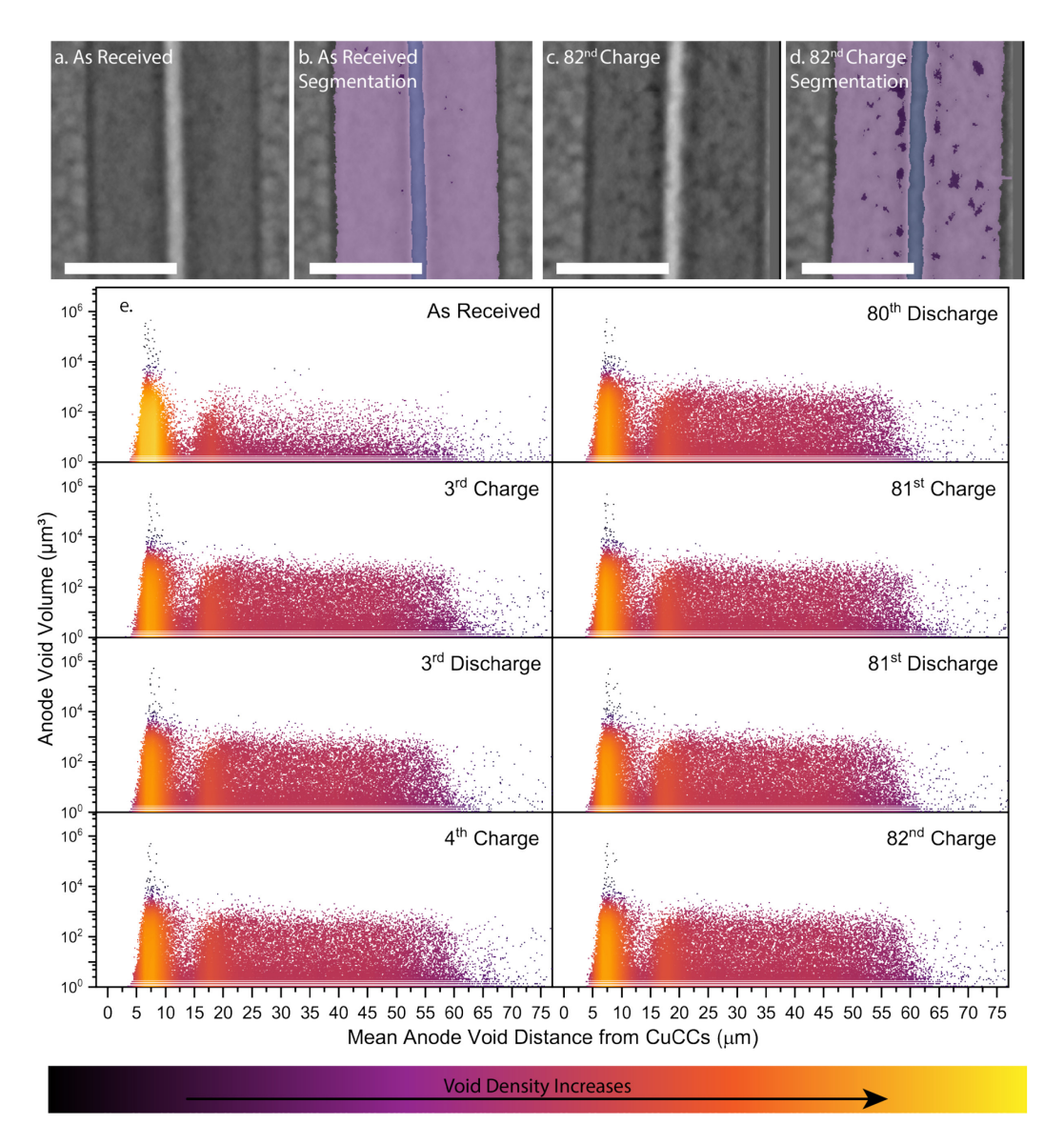


Figure 4. Spatial positioning of anode voids. Reconstructed microCT data from the as-received (a) and 82<sup>nd</sup> charge (c) with the corresponding deep learning segmentation (b and d), scale bars = 100μm. (e) Density scatter plots of anode voids showing void volume with respect to mean void distance away from the Cu CCs.

A visual comparison of a portion of the dual anode coating in the as-received state and after 82 charge-discharge cycles are shown in Figures 4a and c. The corresponding segmentation of the anode coating, anode voids, and Cu CCs are reported adjacent in Figures 4b and d. Qualitatively,

a significant texture difference in the anode coating after 82 cycles is observed, confirming the increase in the total void fraction discussed above. Slight beam hardening artifacts appear as a 5-micron glow on either side of the Cu CCs, reducing the visibility of voids in that region. There is also a darker intensity region on either side of the beam hardening region. Both the beam hardening glow and shadowing artifact are caused by the brightly attenuating pixels from the Cu, which is a heavy absorber. In creating the segmentation training data, two different thresholding ranges are used when designating the voids to prevent segmentation error in this darker region. A higher intensity cutoff is used for the voids closer to the current collector and a lower cutoff for the remaining body of the coating. Accuracy evaluation of the void segmentation is done by carefully comparing the as-received and cycled anode coatings as described in the experimental details.

Density scatter plots shown in Figure 4e are generated from the Cu CC EDM. They offer the respective mean position away from the Cu CCs of the segmented and itemized voids. The y-axis indicates individual void volume on a logarithmic scale. Each data point is color-coded depending on the density of the voids in that area. In the as-received state, the highest density of voids is observed by the current collector, which also has a slightly higher volume per void. This observation suggests the existence of delamination either during fabrication or during formation. The localized delamination near the current collectors could impose penalties on available capacity through reduced electronic percolation. Upon the 3<sup>rd</sup> charge, an overall increase in larger voids across the entire thickness of the anode coating is shown. Voids localized within the first 10 microns away from the Cu CCs spread approximately five additional microns from the as-received state. The positions of these denser void regions stay relatively constant upon 3<sup>rd</sup> discharge through 82<sup>nd</sup> charge. These initial localized voids at the current collector and electrode interface could have appeared due to mechanical stress from the electrode winding process, perhaps aggravated by

outgassing during formation.<sup>29</sup> Similar observations were made at a lower spatial resolution in a previous microCT study of 18650 batteries where cracks in the electrode were formed during the winding process at the corners of a current collector mesh, which subsequently propagated during cycling.<sup>10</sup> There is also a denser region of voids between 15-20 microns away from the current collectors in the as-received state, which grows and increases in density upon further cycling which has not been observed previously.

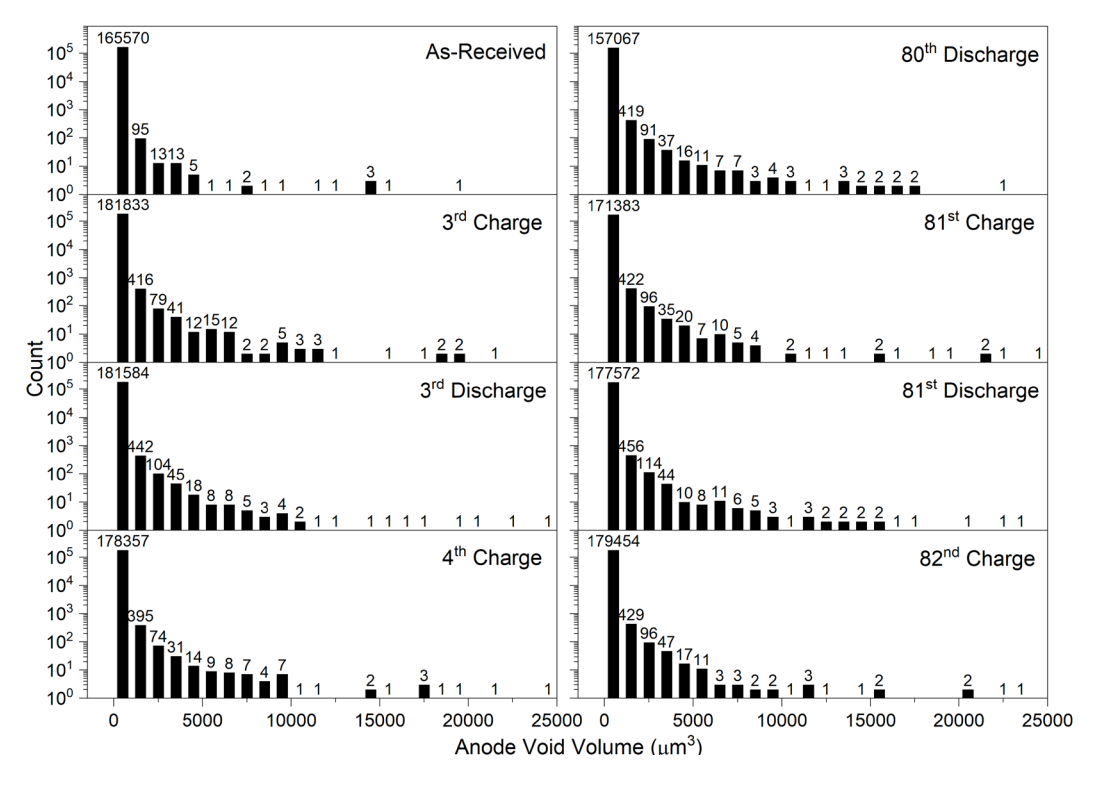


Figure 5. Histograms of the anode void volumes from the as-received state, 3<sup>rd</sup> charge to 4<sup>th</sup> charge, and 80<sup>th</sup> discharge to 82<sup>nd</sup> charge.

Histograms relating to the anode void volume at distinct cycling points are reported in Figure 5. From the as-received state to the  $3^{rd}$  charge, an increase in voids with volume above  $15000 \, \mu m^3$  is observed. When comparing the volume histograms and density scatter plots in Figure 4, it is apparent that the mean positions of these large voids occur within the first 5-10  $\mu$ m away from the current collector as part of the delamination of the electrode coating. Breathing of the electrode

and void network is observed when looking at the larger anode voids above  $10000~\mu m^3$ . The  $20000~\mu m^3$  voids in the  $3^{rd}$  charge reduce in volume upon  $3^{rd}$  discharge, accompanied by an increase in smaller void volumes below  $10000~\mu m^3$ . Void compression and dilation trending with charge and discharge are additionally seen in the two cycles from the  $80^{th}$  discharge to the  $82^{nd}$  charge. These phenomena can be visualized in the supplemental videos when focusing on the distinctly larger voids.

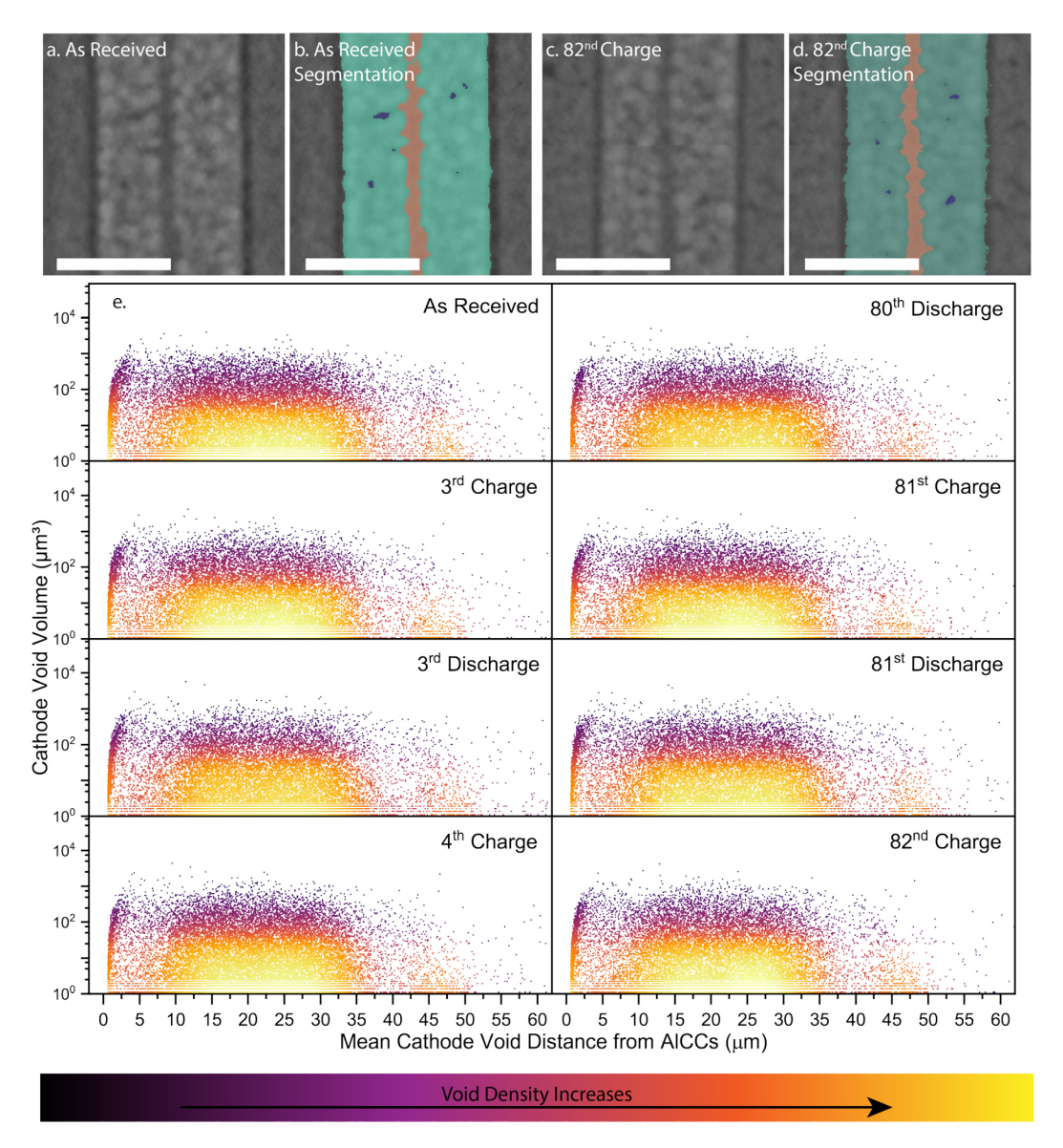


Figure 6. Spatial positioning of cathode voids. Reconstructed microCT data from the as-received (a) and  $82^{nd}$  charge (c) with the corresponding deep learning segmentation (b and d), scale bars =  $100 \ \mu m$ . (e) Density scatter plots of cathode void showing void volume with respect to mean void distance away from the Al CCs.

Upon visual inspection of the reconstructed microCT data of the cathode coating from the asreceived and cycled battery in the 82<sup>nd</sup> charged state (Figures 6a and c), no clear differences in void size and distribution can be resolved. Corresponding segmentation of the cathode coating, cathode voids, and Al CCs are seen in Figures 6b and d. A careful distinction is made in segmenting the darker pixel void regions from the conductive binder matrix that appear darker than the NCA particles but slightly lighter than the void regions.

In Figure 6e, the distribution of cathode voids is dispersed throughout the entire cathode layer, in contrast with the systematic trends observed for the anode. There is a slightly denser population within the first ~3 µm away from the Al CCs, but there is insufficient precision in the segmentation to confirm its existence with complete certainty. False positive and negative segmentation error in this region is shown in Figure S3, which serves to visualize the uncertainty at the interface of the low contrast Al CCs and electrode. The as-received sample has a denser population of voids throughout the entire cathode electrode coating layer compared to the cycled material, which accounts for the higher percentage of voids seen in the percentage totals in Figure 3.

Similar to the observed trend in the anode scatter plots in Figures 4 and 5, when the cathode scatter plots in Figure 6 are overlaid, there is a slight "breathing" of the void volume distribution upon charge and discharge, which is visually confirmed in the supplemental videos. The individual void volumes shift down upon charge and increase upon discharge, a trend opposite to the anode. This observation is explained by the compression of the active material and carbon-binder matrix upon delithiation, reducing both individual and, state above, total void volume. The decrease in void volume can significantly affect both lithium and electronic transport. The observation in reduced porosity may hint at a collapse in the conductive binder matrix, reducing electrolyte infiltration and Li<sup>+</sup> ion conductivity. Cathode particles are known to fracture during cycling, especially at high rates. Such particle fragments could be anticipated to rearrange into the open void network, while newly exposed NCA primary particle surfaces cause an increase in the formation of interphasial layers, further filling empty voids. Unfortunately, these phenomena

would not be observable at the resolution limit of the microCT experiment used in this study, namely  $\sim 3~\mu m$ . The resulting tighter packed electrode structure is visible in the reduction in baseline electrode thickness in Figure 2h.

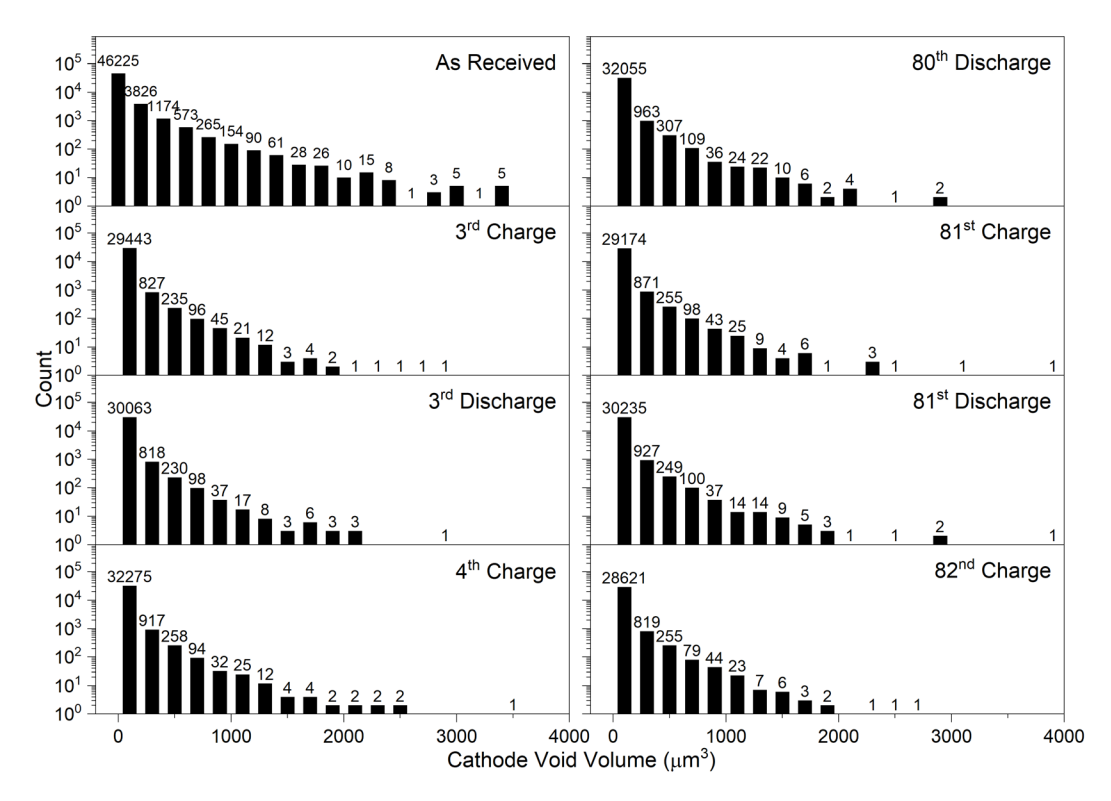


Figure 7. Cathode void histograms from the as-received state, 3<sup>rd</sup> charge to 4<sup>th</sup> charge, and 80<sup>th</sup> discharge to 82<sup>nd</sup> charge.

The cathode void histograms in Figure 7 show the as-received state having a significant number of larger voids above 2000 micron<sup>3</sup> that decreased upon the 3<sup>rd</sup> charge. The larger voids shown in the histograms are approximately five times smaller in volume than the reported anode voids in Figure 7. These initial voids indicate further evidence of the manufactured porosity of the cathode electrode that is optimized through the coating and calendering process being reduced significantly through fast rate charge cycling. The breathing of the cathode and void network seen in Figure 6 is better visualized in Figure 7 from the 80<sup>th</sup> discharge to 82<sup>nd</sup> charge. This effect is seen in the reduction of voids around 3000 µm<sup>3</sup> to lower volumes closer to 2000 µm<sup>3</sup> and below.

#### 4. CONCLUSIONS:

Operando microCT of the fast charging of 18650 batteries is an extremely valuable tool for diagnosing the internal degradation mechanisms that affect the overall capacity retention and battery performance. The tool provides adequate resolution over a statistically relevant sized field of view. The appropriate time resolution was also easily achievable with the high flux of a synchrotron X-ray source. This type of evaluation is essential in observing the challenges commercial batteries still face when exposed to actual cycling conditions relevant to electric vehicles.

Objectively quantifying morphological changes requires accurate segmentation of all the relevant internal battery components and void network, which becomes challenging in an operando data set with approximately 50 tomograms with evolving parameters. We developed a Deep Learning model that required only 17 representative training slices to create a robust segmentation to solve this issue. After the segmentation model was applied, EDM was used to evaluate the spatial trends of internal degradation further. We established that the reversible and irreversible expansion of both the anode and the cathode coating layers upon Li<sup>+</sup> de/intercalation could be followed using EDM calculated from the corresponding current collectors. The ability to measure dilation trends in both electrodes simultaneously while deconvoluting individual contributions increases the flexibility of standard dilatometry experiments previously limited to soft walled halfcell battery architectures. The EDM method takes advantage of the full voxel resolution of the original imaging technique without additional user manipulation or processing power. With the massive size of data collected from computed tomography imaging techniques, development in novel automated quantification analysis techniques is required to take advantage of the complete dataset.

EDM also proved helpful in tracking where voids are forming spatially in both electrode coatings. Localized voids close to the Cu CCs in the anode that increased upon further cycling showed evidence of electrode delamination. At the same time, the dilation of the anode showed high reversibility, although it was accompanied by irreversible increases of void fraction, yet spread over the thickness of the electrode. A general rise in baseline thickness was calculated in the cathode coating layers during the 80<sup>th</sup> to 82<sup>nd</sup> cycle. In contrast, a decrease in voids in the body of the cathode was observed overall. The direct visualization of the opposing trends in cathode and anode dilation and porosity in a cylindrical cell format have not been reported previously. Using imaging techniques with a higher spatial resolution will provide further insight into how cathode particle microcracking contributes to this decreased electrode porosity. The workflow of the Deep Learning segmentation and EDM techniques proposed here could be easily tuned to higher resolution imaging techniques. The quantification of degradation spatially at the single-particle nanoscale to the micro-multielectrode scale, with varying cycling conditions, provides a path for future experiments.

#### 5. ACKNOWLEDGMENTS:

This work was primarily supported by the National Science Foundation, under award CBET-2022723. The research was initiated through an appointment with the Energy Efficiency & Renewable Energy (EERE) Energy Storage Internship Program sponsored by the U.S. Department of Energy (DOE), EERE Advanced Manufacturing Office (AMO). This program is administered by the Oak Ridge Institute for Science and Education (ORISE) for the DOE. ORISE is managed by ORAU. All opinions expressed in this paper are the author's and do not necessarily reflect the policies and views of DOE, ORAU, or ORISE.

The authors wish to thank the beamline scientist, Dr. Xianghui Xiao, now at Brookhaven National Laboratory, for his invaluable help before, during, and after the beamtime. Use of the Advanced Photon Source was supported by the U. S. Department of Energy, Office of Science, Office of Basic Energy Sciences, under Contract No. DE-AC02-06CH11357. This research used resources of the Stanford Synchrotron Radiation Lightsource, SLAC National Accelerator Laboratory, which is supported by the U.S. Department of Energy, Office of Science, Office of Basic Energy Sciences under Contract No. DE-AC02-76SF00515.

## 6. ABBREVIATIONS:

CBM Conductive Carbon Matrix

EDM Euclidean Distance Mapping

MicroCT X-Ray Microcomputed Tomography

ORS Object Research Systems

CNN Convolutional Neural Network

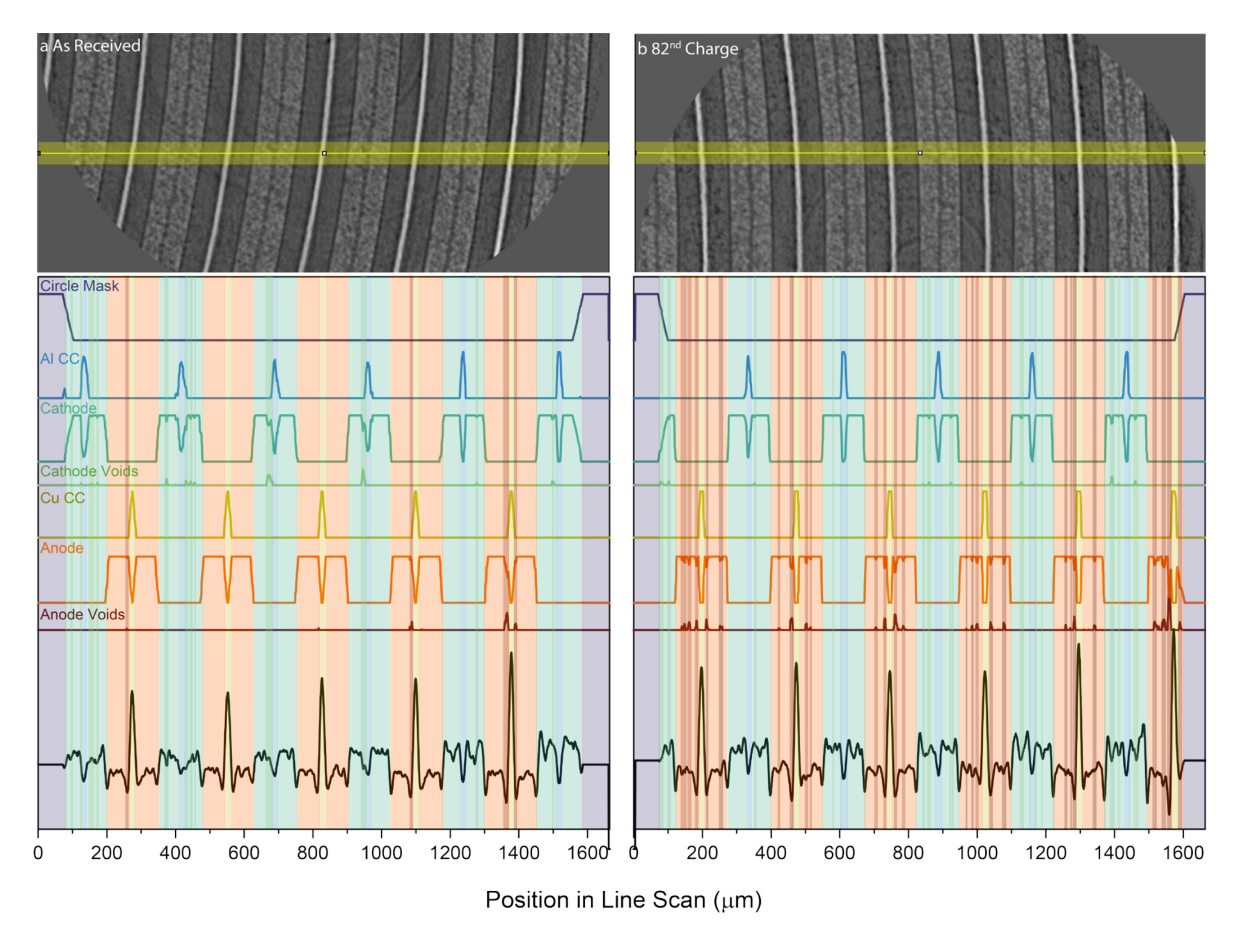
CUDA Compute Unified Device Architecture

GUI Graphical User Interface

CC Current Collector

NCA LiNi<sub>0.8</sub>Co<sub>0.15</sub>Al<sub>0.05</sub>O<sub>2</sub>

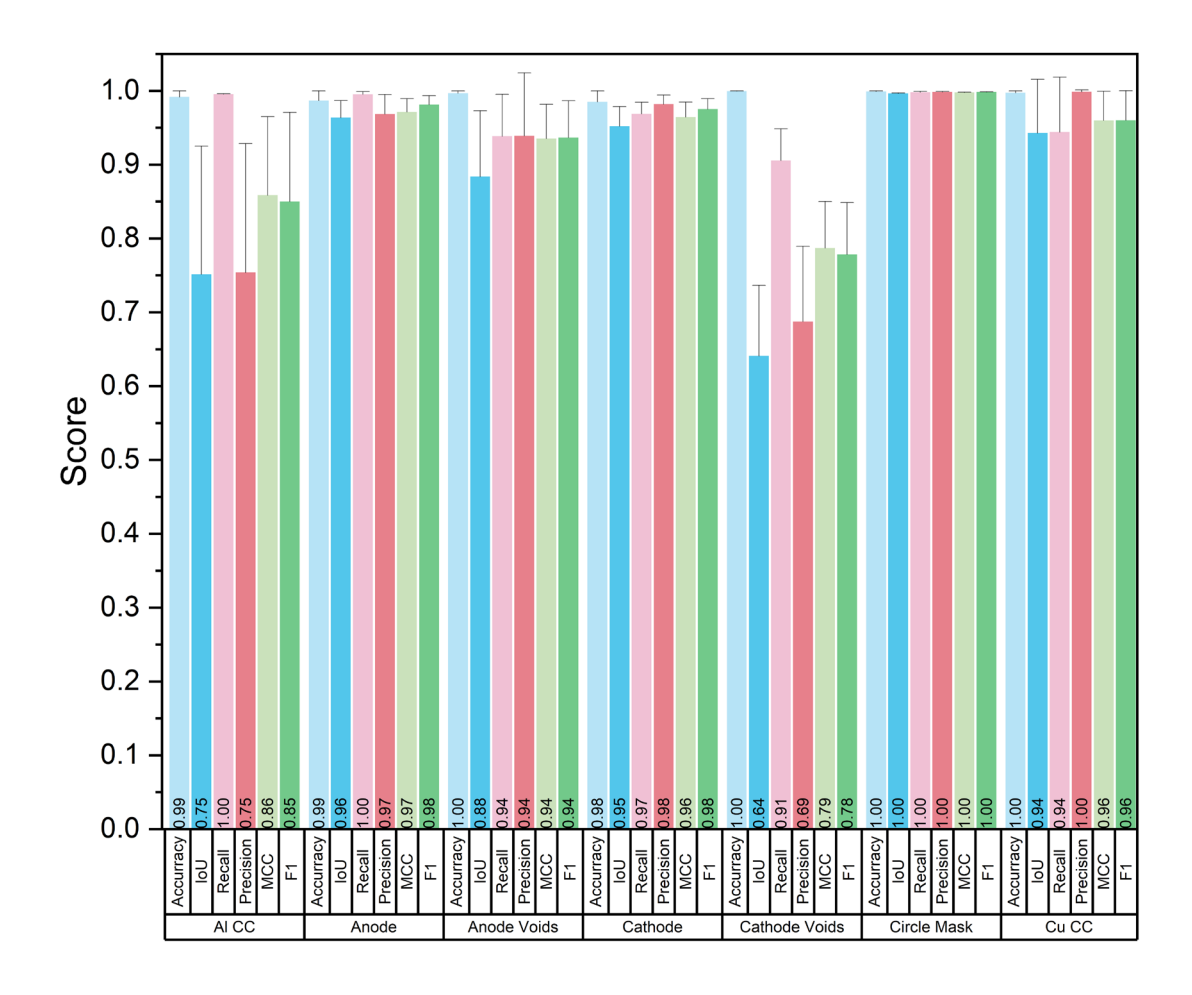
## SUPPLEMENTARY INFORMATION



S 1. Line scans through portions of typical reconstructed slices from the initial as-received state (a) and the 82<sup>nd</sup> charge state (b) of the 18650 batteries received from Lucid Motor Company. Below each slice are the corresponding 50-pixel wide linescans of the semantic segmentation assigned components (colored and labeled) and the raw greyscale intensity (black).

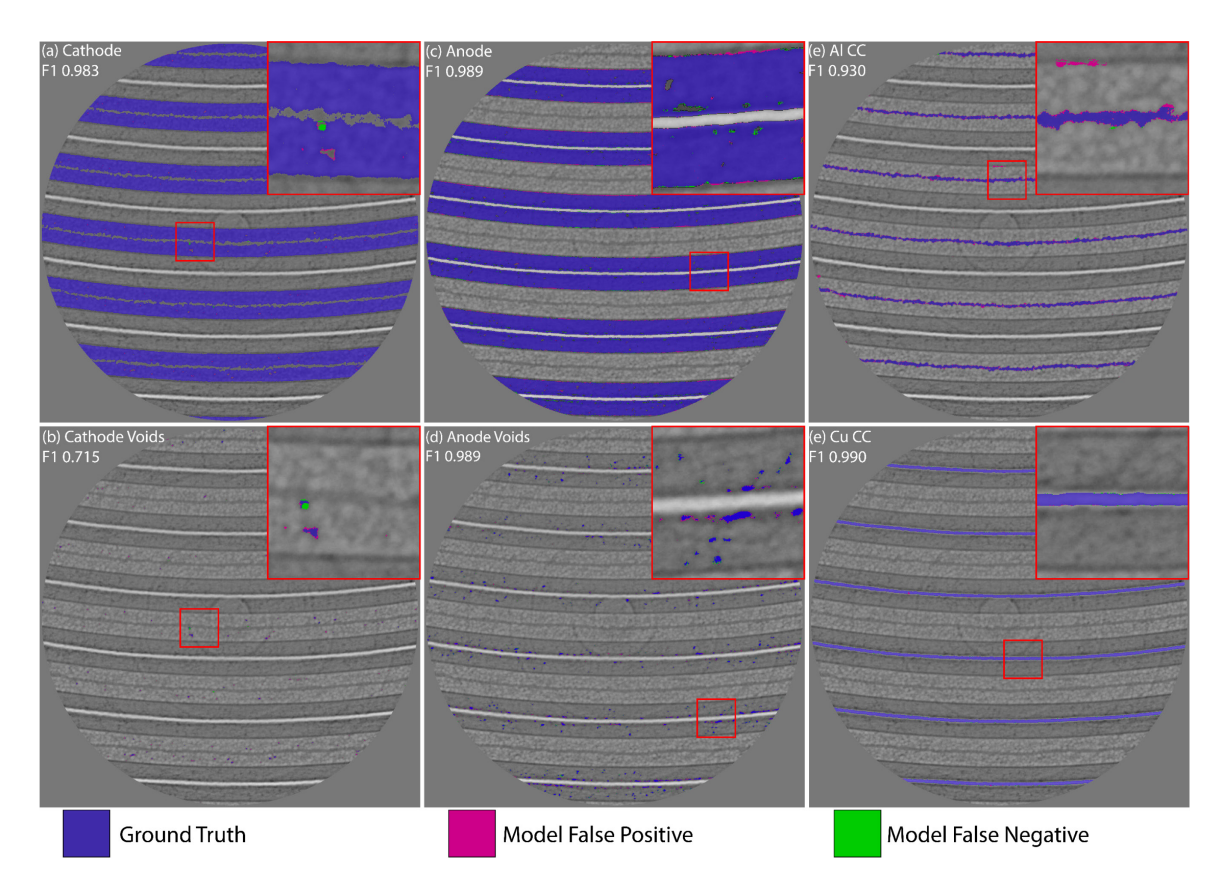
Table S1. Deep Learning Training Parameters

Input Size (pixels)	128
Stride-to-input Ratio	0.5
Batch Size	32
Number of Epochs	45
Loss Function	Categorical cross-entropy
Optimizer Algorithm	Adadelta <sup>36</sup>

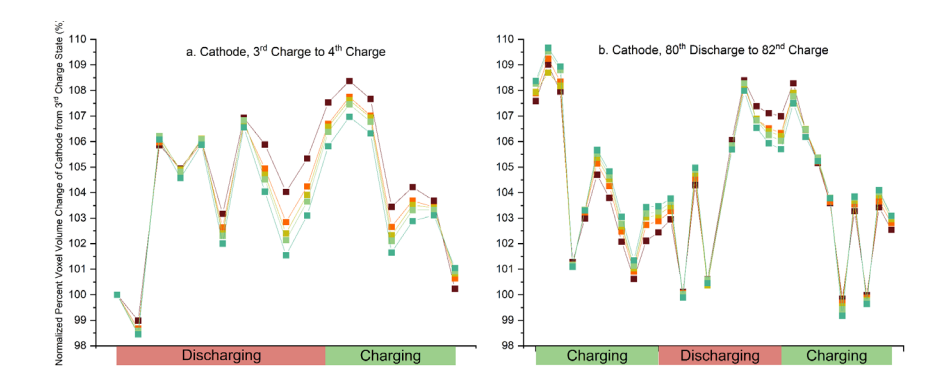


S 2. Six common segmentation model evaluation scores are reported for the model output: Accuracy, Intersection-Over-Union (IoU), Recall, Precision, Matthews Correlation Coefficient

(MCC), and F1 scores for the seven segmented components: Al CC, anode, anode voids, cathode, cathode voids, circle mask, and Cu CC.



S 3. Maps of false positive/negatives in the segmentation model, overlaid on the ground truth segmentation for each component. F1 scores are presented for each component.



S 4. Voxel volume percentages normalized to the first data point at the 3<sup>rd</sup> charge state of the individual cathode electrode layers. The profiles of voxel volume change are the same as the tracked thickness graphs in Figure 2 g-h.

# **Supplementary Movies Included in File**

## **REFERENCES:**

- (1) Sun, G.; Sui, T.; Song, B.; Zheng, H.; Lu, L.; Korsunsky, A. M. On the Fragmentation of Active Material Secondary Particles in Lithium Ion Battery Cathodes Induced by Charge Cycling. *Extrem. Mech. Lett.* **2016**, *9* (March), 449–458. https://doi.org/10.1016/j.eml.2016.03.018.
- (2) Radin, M. D.; Hy, S.; Sina, M.; Fang, C.; Liu, H.; Vinckeviciute, J.; Zhang, M.; Whittingham, M. S.; Meng, Y. S.; Van der Ven, A. Narrowing the Gap between Theoretical and Practical Capacities in Li-Ion Layered Oxide Cathode Materials. *Adv. Energy Mater.* **2017**, *7* (20), 1–33. https://doi.org/10.1002/aenm.201602888.
- (3) Lin, F.; Zhao, K.; Liu, Y. Heterogeneous Reaction Activities and Statistical Characteristics of Particle Cracking in Battery Electrodes. *ACS Energy Lett.* **2021**, *6* (11), 4065–4070. https://doi.org/10.1021/acsenergylett.1c02135.
- (4) Xu, R.; Yang, Y.; Yin, F.; Liu, P.; Cloetens, P.; Liu, Y.; Lin, F.; Zhao, K. Heterogeneous Damage in Li-Ion Batteries: Experimental Analysis and Theoretical Modeling. *J. Mech. Phys. Solids* **2019**, *129* (2019), 160–183. https://doi.org/10.1016/j.jmps.2019.05.003.
- (5) Boyce, A. M.; Martínez-Pañeda, E.; Wade, A.; Zhang, Y. S.; Bailey, J. J.; Heenan, T. M. M.; Brett, D. J. L.; Shearing, P. R. Cracking Predictions of Lithium-Ion Battery Electrodes by X-Ray Computed Tomography and Modelling. *J. Power Sources* **2022**, *526* (January). https://doi.org/10.1016/j.jpowsour.2022.231119.
- (6) Miller, D. J.; Proff, C.; Wen, J. G.; Abraham, D. P.; Bareño, J. Observation of Microstructural Evolution in Li Battery Cathode Oxide Particles by in Situ Electron Microscopy. *Adv. Energy Mater.* **2013**, *3* (8), 1098–1103. https://doi.org/10.1002/aenm.201300015.

- (7) Kleiner, K.; Jakes, P.; Scharner, S.; Liebau, V.; Ehrenberg, H. Changes of the Balancing between Anode and Cathode Due to Fatigue in Commercial Lithium-Ion Cells. *J. Power Sources* **2016**, *317*, 25–34. https://doi.org/10.1016/j.jpowsour.2016.03.049.
- (8) Jiang, Z.; Li, J.; Yang, Y.; Mu, L.; Wei, C.; Yu, X.; Pianetta, P.; Zhao, K.; Cloetens, P.; Lin, F.; Liu, Y. Machine-Learning-Revealed Statistics of the Particle-Carbon/Binder Detachment in Lithium-Ion Battery Cathodes. *Nat. Commun.* **2020**, *11* (1). https://doi.org/10.1038/s41467-020-16233-5.
- (9) Daemi, S. R.; Tan, C.; Volkenandt, T.; Cooper, S. J.; Palacios-Padros, A.; Cookson, J.; Brett, D. J. L.; Shearing, P. R. Visualizing the Carbon Binder Phase of Battery Electrodes in Three Dimensions. *ACS Appl. Energy Mater.* **2018**, *I* (8), 3702–3710. https://doi.org/10.1021/acsaem.8b00501.
- (10) Ziesche, R. F.; Arlt, T.; Finegan, D. P.; Heenan, T. M. M.; Tengattini, A.; Baum, D.; Kardjilov, N.; Markötter, H.; Manke, I.; Kockelmann, W.; Brett, D. J. L.; Shearing, P. R. 4D Imaging of Lithium-Batteries Using Correlative Neutron and X-Ray Tomography with a Virtual Unrolling Technique. *Nat. Commun.* **2020**, *11* (1), 1–11. https://doi.org/10.1038/s41467-019-13943-3.
- (11) Wang, P.; Chen, P.; Yuan, Y.; Liu, D.; Huang, Z.; Hou, X.; Cottrell, G. Understanding Convolution for Semantic Segmentation. *Proc. 2018 IEEE Winter Conf. Appl. Comput. Vision, WACV 2018* **2018**, *2018-Janua*, 1451–1460. https://doi.org/10.1109/WACV.2018.00163.
- (12) Smith, P.; Reid, D. B.; Environment, C.; Palo, L.; Alto, P.; Smith, P. L. Otsu\_1979\_otsu\_method. *IEEE Trans. Syst. Man. Cybern.* **1979**, *C* (1), 62–66. https://doi.org/10.1109/TSMC.1979.4310076.

- (13) Liu, Y.; Zhao, T.; Ju, W.; Shi, S.; Shi, S. Materials Discovery and Design Using Machine Learning. *J. Mater.* **2017**, *3* (3), 159–177. https://doi.org/10.1016/j.jmat.2017.08.002.
- (14) Li, S.; Jiang, Z.; Han, J.; Xu, Z.; Wang, C.; Huang, H.; Yu, C.; Lee, S. J.; Pianetta, P.; Ohldag, H.; Qiu, J.; Lee, J. S.; Lin, F.; Zhao, K.; Liu, Y. Mutual Modulation between Surface Chemistry and Bulk Microstructure within Secondary Particles of Nickel-Rich Layered Oxides. *Nat. Commun.* **2020**, *11* (1), 1–9. https://doi.org/10.1038/s41467-020-18278-y.
- (15) Xia, S.; Mu, L.; Xu, Z.; Wang, J.; Wei, C.; Liu, L.; Pianetta, P.; Zhao, K.; Yu, X.; Lin, F.; Liu, Y. Chemomechanical Interplay of Layered Cathode Materials Undergoing Fast Charging in Lithium Batteries. *Nano Energy* **2018**, *53* (August), 753–762. https://doi.org/10.1016/j.nanoen.2018.09.051.
- (16) Wong, H. S.; Buenfeld, N. R. Euclidean Distance Mapping for Computing Microstructural Gradients at Interfaces in Composite Materials. *Cem. Concr. Res.* **2006**, *36* (6), 1091–1097. https://doi.org/10.1016/j.cemconres.2005.10.003.
- (17) Ender, M.; Joos, J.; Carraro, T.; Ivers-Tiffée, E. Quantitative Characterization of LiFePO 4 Cathodes Reconstructed by FIB/SEM Tomography . *J. Electrochem. Soc.* **2012**, *159* (7), A972–A980. https://doi.org/10.1149/2.033207jes.
- (18) Ender, M.; Joos, J.; Weber, A.; Ivers-Tiffée, E. Anode Microstructures from High-Energy and High-Power Lithium-Ion Cylindrical Cells Obtained by X-Ray Nano-Tomography. *J. Power Sources* **2014**, *269*, 912–919. https://doi.org/10.1016/j.jpowsour.2014.07.070.

- (19) Almar, L.; Joos, J.; Weber, A.; Ivers-Tiffée, E. Microstructural Feature Analysis of Commercial Li-Ion Battery Cathodes by Focused Ion Beam Tomography. *J. Power Sources* **2019**, 427 (March), 1–14. https://doi.org/10.1016/j.jpowsour.2019.04.019.
- (20) Du, W.; Owen, R. E.; Jnawali, A.; Neville, T. P.; Iacoviello, F.; Zhang, Z.; Liatard, S.; Brett, D. J. L.; Shearing, P. R. In-Situ X-Ray Tomographic Imaging Study of Gas and Structural Evolution in a Commercial Li-Ion Pouch Cell. *J. Power Sources* **2022**, *520* (December 2021), 230818. https://doi.org/10.1016/j.jpowsour.2021.230818.
- (21) Krygier, M. C.; LaBonte, T.; Martinez, C.; Norris, C.; Sharma, K.; Collins, L. N.; Mukherjee, P. P.; Roberts, S. A. Quantifying the Unknown Impact of Segmentation Uncertainty on Image-Based Simulations. *Nat. Commun.* **2021**, *12* (1), 5414. https://doi.org/10.1038/s41467-021-25493-8.
- (22) Ebner, M.; Marone, F.; Stampanoni, M.; Wood, V. Visualization and Quantification of Electrochemical and Mechanical. *Science* (80-. ). **2013**, 342 (November), 716–721.
- (23) Gürsoy, D. D.; De Carlo, F.; Xiao, X.; Jacobsen, C. TomoPy: A Framework for the Analysis of Synchrotron Tomographic Data. *J. Synchrotron Radiat.* **2014**, *21* (5), 1188–1193. https://doi.org/10.1107/S1600577514013939.
- (24) Palenstijn, W. J.; Sijbers, J.; Pelt, D. M.; Gürsoy, D.; Palenstijn, W. J.; Sijbers, J.; De Carlo, F.; Batenburg, K. J. Integration of TomoPy and the ASTRA Toolbox for Advanced Processing and Reconstruction of Tomographic Synchrotron Data. *J. Synchrotron Radiat.* **2016**, *23* (3), 842–849. https://doi.org/10.1107/S1600577516005658.

- (25) Dowd, B. A.; Campbell, G. H.; Marr, R. B.; Nagarkar, V. V.; Tipnis, S. V.; Axe, L.; Siddons, D. P. Developments in Synchrotron X-Ray Computed Microtomography at the National Synchrotron Light Source. In *Developments in X-Ray Tomography II*; Bonse, U., Ed.; 1999; Vol. 3772, pp 224–236. https://doi.org/10.1117/12.363725.
- (26) Ronneberger, O.; Fischer, P.; Brox, T. U-Net: Convolutional Networks for Biomedical Image Segmentation. *Lect. Notes Comput. Sci. (including Subser. Lect. Notes Artif. Intell. Lect. Notes Bioinformatics)* **2015**, *9351*, 234–241. https://doi.org/10.1007/978-3-319-24574-4 28.
- (27) Yong, Guillaume Lemaitre-Eng Wei, and G. L. Evaluation Measures for Segmentation. *matrix* **2016**, *I* (1), 2.
- (28) Prezas, P. D.; Somerville, L.; Jennings, P.; McGordon, A.; Basco, J. K.; Duong, T.; Bloom, I. Effect of Fast Charging of Lithium-Ion Cells: Performance and Post-Test Results. *SAE Tech. Pap.* **2016**. https://doi.org/10.4271/2016-01-1194.
- (29) Michael, H.; Iacoviello, F.; Heenan, T. M. M.; Llewellyn, A.; Weaving, J. S.; Jervis, R.; Brett, D. J. L.; Shearing, P. R. A Dilatometric Study of Graphite Electrodes during Cycling with X-Ray Computed Tomography. *J. Electrochem. Soc.* **2021**, *168* (1), 010507. https://doi.org/10.1149/1945-7111/abd648.
- (30) Bauer, M.; Wachtler, M.; Stöwe, H.; Persson, J. V.; Danzer, M. A. Understanding the Dilation and Dilation Relaxation Behavior of Graphite-Based Lithium-Ion Cells. *J. Power Sources* **2016**, *317*, 93–102. https://doi.org/10.1016/j.jpowsour.2016.03.078.
- (31) Robert, R.; Bunzli, C.; Berg, E. J.; Novák, P. Activation Mechanism of LiNi0.80Co0.15Al0.05O2: Surface and Bulk Operando Electrochemical, Differential

Electrochemical Mass Spectrometry, and x-Ray Diffraction Analyses. *Chem. Mater.* **2015**, *27* (2), 526–536. https://doi.org/10.1021/cm503833b.

- (32) Yu, D. Y. W.; Zhao, M.; Hoster, H. E. Suppressing Vertical Displacement of Lithiated Silicon Particles in High Volumetric Capacity Battery Electrodes. *ChemElectroChem* **2015**, *2* (8), 1090–1095. https://doi.org/10.1002/celc.201500133.
- (33) Koerver, R.; Zhang, W.; De Biasi, L.; Schweidler, S.; Kondrakov, A. O.; Kolling, S.; Brezesinski, T.; Hartmann, P.; Zeier, W. G.; Janek, J. Chemo-Mechanical Expansion of Lithium Electrode Materials-on the Route to Mechanically Optimized All-Solid-State Batteries. *Energy Environ. Sci.* **2018**, *11* (8), 2142–2158. https://doi.org/10.1039/c8ee00907d.
- (34) McShane, E. J.; McShane, E. J.; Colclasure, A. M.; Brown, D. E.; Brown, D. E.; Konz, Z. M.; Konz, Z. M.; Smith, K.; McCloskey, B. D.; McCloskey, B. D. Quantification of Inactive Lithium and Solid-Electrolyte Interphase Species on Graphite Electrodes after Fast Charging. *ACS Energy Lett.* **2020**, *5* (6), 2045–2051. https://doi.org/10.1021/acsenergylett.0c00859.
- (35) Mao, C.; Ruther, R. E.; Li, J.; Du, Z.; Belharouak, I. Identifying the Limiting Electrode in Lithium Ion Batteries for Extreme Fast Charging. *Electrochem. commun.* **2018**, *97* (September), 37–41. https://doi.org/10.1016/j.elecom.2018.10.007.
  - (36) Zeiler, M. D. ADADELTA: An Adaptive Learning Rate Method. 2012.